Noise Reduction in PET Attenuation Correction by Maximum Likelihood Histogram Sharpening of Attenuation Images

Julie C. Price, Stephen L. Bacharach, Nanette Freedman and Richard E. Carson

PET Department and Nuclear Medicine Department, National Institutes of Health, Bethesda, Maryland

A new method for PET transmission data processing was developed and found to reduce transmission noise in ^{18}F-FDG cardiac emission images. This method is based on a model that describes the measured attenuation image histogram as some unknown true underlying histogram, blurred by noise. **Methods:** Emission data from an elliptical phantom (cardiac insert) and three humans were reconstructed using transmission data of varying duration with varying levels of smoothing. Biases and noise levels (cardiac sector analysis) were evaluated for the phantom (simulated replicates) and human emission images. **Results:** The estimated attenuation histograms typically displayed three distinct peaks corresponding to air, lung and soft tissue without a priori assumptions of the underlying μ values. This method effectively sharpened the histogram peaks and performed well for the phantom and human data. For intermediate transmission noise levels, biases in the phantom sector values were <4%. The human sector results were more variable but consistent with the phantom results. Noise reduction (~30%) was demonstrated across all smooth levels for the phantom data. **Conclusion:** This histogram sharpening method introduces only small bias in the cardiac sector values while achieving an increase in effective transmission scan time of 50–100%. Alternatively, histogram sharpening permits less transmission data smoothing without increased noise.

Key Words: PET transmission noise; noise reduction; attenuation histogram; fluorine-18-FDG

J Nucl Med 1996; 37:786–794

A fundamental problem in emission computed tomography is the attenuation of photons in the object of interest. PET attenuation correction is performed using either calculated or measured methods. Calculated methods most often assume a uniform attenuating medium and require that the object size, shape and position be determined. Such methods have most commonly been used for brain imaging. The measured method is most applicable for cardiac imaging due to the complex attenuating media in the thorax. The measured method involves the acquisition of a long duration blank scan with nothing in the scanner (B) and a shorter duration transmission scan with the subject in the scanner (T). The ratio of these data for each projection line (B/T) yields attenuation correction factors (ACFs) by which the emission data are multiplied prior to reconstruction.

Measured methods have the problem of limited statistics and, consequently, the ACFs add noise to the corrected emission image (1–3). Therefore, it is common to smooth the transmission data prior to correction. More sophisticated methods have also been developed to reduce noise in the ACFs by processing the reconstructed attenuation image (4–6). These methods are of practical interest because they may permit the use of transmission scans of short duration. These techniques and the

method presented here involve: (a) reconstruction of an attenuation image, (b) implementation of a specific algorithm to reassign attenuation coefficients (μ) and (c) reprojection of the resulting attenuation image to obtain new ACFs for emission reconstruction.

The earliest reprojection method was described by Huang et al. (4). In this method, regions were identified on the attenuation image using an edge-finding algorithm and average regional μ values were determined from the original image. The μ values in a region were reassigned to the appropriate average to provide a new image with discrete and uniform μ levels. Xu et al. (5) segmented the attenuation image into uniform regions of air, lung and soft tissue based on the image histogram. This method was modified by Meikle et al. (6) to allow for a more relaxed segmentation by describing the attenuation image histogram as three Gaussian functions. These methods commonly require assumptions about the underlying distribution of μ values.

In this work, we present a method that: (a) does not require assumptions about the underlying distribution of μ values in the attenuation image and (b) explicitly accounts for noise in the attenuation image. A model is developed to describe the histogram of the attenuation image in terms of a true underlying histogram blurred by noise. The parameters of the noise function are determined from the properties of the attenuation image. The processing method consists of three steps. First, a maximum likelihood algorithm is used to estimate the true image histogram from the measured histogram. This processing results in an effective sharpening of the attenuation histogram. Second, the pixel μ values are reassigned to produce an attenuation image with a histogram that matches the estimated histogram. Third, the new attenuation image is reprojected to obtain the new ACFs.

The bias and variability of cardiac emission quantification using histogram sharpening was evaluated with phantom experiments and the method was applied to studies in human subjects in order to assess its clinical utility.

METHODS

Scans were acquired on a Posicam 6.5 (Positron Corp., Houston, TX) whole-body PET scanner (in-plane resolution: 6.3 mm FWHM (ramp filter), axial slice width: 12.5 mm FWHM). Twenty-one slices (pixel size: 1.7 mm for 256 × 256 images) were acquired (slice separation: 5.1 mm). The blank and transmission data were obtained using a rotating [68]Ge pin source (2–3 mCi) with sinogram masking.

Phantom Data. Data were acquired using an elliptical (Data Spectrum® Lung, Chapel Hill, NC) phantom with fillable lungs, a cylindrical spine simulator and a cardiac phantom with chambers to simulate the left ventricular cavity and myocardium. Radioactivity (^{18}F) was added to the phantom background (1.3 μCi/ml) and myocardial chamber (7.5 μCi/ml) for a background:myocardium

ratio of 15%. Water was used to fill the left ventricular cavity and the lungs were packed with styrofoam beads and water.

One emission scan (80 min), five transmission scans (60 min each) and one blank scan (45 min) were acquired. The phantom remained in the scanner overnight between the emission and transmission scans to permit decay. The transmission scans were summed to provide high-count (total counts in central slice: 4.0×10^7) data that were used to simulate lower count data. Poisson realizations of the summed transmission projection data (120 angles, 256 bins) were simulated by Marsaglia's method (7) to provide 50 transmission scans that correspond to times of 3, 7 and 15 min. The high-count emission data (total counts in central slice: 5.9×10^7) were reconstructed with all transmission datasets. A central slice in which the myocardial radioactivity was most clearly visualized was analyzed.

Human Data. Scans were obtained from ^{18}F-FDG (5 mCi) cardiac studies performed on two patients (coronary artery disease) and one normal volunteer. The protocol included a 15-min transmission scan and a 30-min static emission scan (30 min postinjection). An additional 7-min transmission scan was performed after the 15-min scan for the evaluation of the histogram sharpening method. Seven adjacent slices through the center of the heart were analyzed.

Image Reconstruction. The blank and transmission projection data were smoothed prior to division using a radial Gaussian smooth, at three levels: 11, 9 and 7 mm (FWHM). All attenuation images were reconstructed with a ramp filter (cutoff at Nyquist frequency $= 2.9$ cm^{-1}). The emission data were reconstructed with a Hanning filter (cutoff $=$ Nyquist, order $= 0.75$). Table 1 shows the scheme used to represent the combinations of transmission scan durations and attenuation smooth levels.

Theory

Histogram Model. Figure 1 shows attenuation image histograms from the phantom-based simulations for transmission data of 5-hr, 7-min and 3-min durations with 7-mm smoothing. In the 5-hr histogram, there are three distinct peaks centered at bin (μ) values of 0.002 cm^{-1}, 0.04 cm^{-1}, 0.09 cm^{-1} that correspond to air, lung and soft tissue. These peaks are blurred in the 7-min and 3-min histograms due to noise. Therefore, the measured attenuation pixel value (μ_m) was described in terms of its true underlying pixel value (μ_t) that has been contaminated by noise (e):

$$\mu_m = \mu_t + e. \qquad \text{Eq. 1}$$

The random variables μ_t and e are assumed to be independent where e is normally distributed with mean 0 and variance $\sigma^2(\mu)$. The probability density function of μ_m is the convolution of the densities of μ_t and e. Therefore, the measured attenuation image histogram, m (with n_m bins) has the following expected value:

$$E(m(\mu)) = t(\mu) \otimes c_\mu(x) \qquad \text{Eq. 2}$$

where $t(\mu)$ is the true underlying histogram (with n_t bins) and $c_\mu(x)$ corresponds to a Gaussian noise function.

The attenuation pixel noise is incorporated into the model via $c_\mu(x)$. For the phantom, mean and standard deviation attenuation images were generated from the 50 simulations (at each scan duration and smooth level) and the relationship between μ and σ was evaluated. A linear fit was found to be appropriate:

$$\sigma(\mu) = \sigma_s\mu + \sigma_0. \qquad \text{Eq. 3}$$

For the human data, region-of-interest (ROI) means and standard deviations within each region (pixel-to-pixel standard deviation) were obtained from single attenuation images (at each scan duration and smooth level). Forty circular (2.6 cm diameter) ROIs placed in uniform areas of the attenuation image were used to

TABLE 1
Definitions

Simulations	
Case	Transmission Scan Duration with smoothing FWHM
A, B, C	15, 7, 3 min with 11 mm
D, E, F	15, 7, 3 min with 9 mm
G, H, I	15, 7, 3 min with 7 mm
Histogram Model	
μ_m	Measured pixel value
μ_t	True (noise-free) pixel value
e	Noise term: $\sim N(0, \sigma^2)$
m	Measured attenuation histogram
n_m	Number of bins of measured histogram
t	True attenuation histogram
n_t	Number of bins of estimated true histogram
c_μ	Gaussian noise function
$\sigma(\mu)$	Pixel standard deviation (pixel noise), $\sigma(\mu) = \sigma_s\mu + \sigma_0$
Pixel Remapping	
$F_m(\mu)$	Cumulative probability distribution function of the measured histogram
$F_t(\mu)$	Cumulative probability distribution function of the estimated histogram
μ_r	Remapped pixel value
ϕ	Mapping function applied to μ_m to obtain μ_r
Data Analysis	
PPD_j	Phantom percent difference for each sector j across 50 images
S^R	Mean reference sector counts
S_{ij}	Mean sector counts in phantom realization i, sector j
CV	Sector coefficient of variation (n = 50)
HPD_j	Human percent difference for each sector j across 7 central slices
$\sigma^2_{\Delta T}$	Emission image variance (for a given smooth level)
ΔT	Duration of transmission scan
σ_E	Emission data noise
σ_T	Transmission data noise
T_{HS}	Effective scan duration achieved by histogram sharpening
α	Effective time gain

sample the lungs, heart, soft tissue and outside of the subject. A linear regression of the pixel-to-pixel standard deviation versus mean ROI value, that was obtained from each ROI, provided the values of σ_s and σ_0.

Attenuation Image Processing

Histogram Estimation (Histogram Sharpening). The estimated histogram was determined using a maximum likelihood expectation-maximization (EM) technique similar to that used for image reconstruction (8,9). The measured histogram (m_i, $i = 1, \ldots, n_m$) has a multinomial distribution and given the large number of pixels in the image, this was approximated by a Poisson distribution:

$$m_i \sim \text{Poisson}\left(\sum_{j=1}^{n_t} c_{ij}t_j\right) \qquad \text{Eq. 4}$$

where t_j is the true pixel count in bin j and c_{ij} is the noise function of Equation 2:

$$c_{ij} = \frac{1}{\sqrt{2\pi\sigma^2(\mu_j)}} e^{-((\mu_i - \mu_j)^2/2\sigma^2(\mu_j))} \qquad \text{Eq. 5}$$

with attenuation bin values μ_i and μ_j. The EM algorithm at the nth iteration is:

$$\hat{t}_j^{n+1} = \frac{\hat{t}_j^n}{\sum_i c_{ij}} \sum_i c_{ij} \frac{m_i}{\sum_k c_{ik}\hat{t}_k^n}. \qquad \text{Eq. 6}$$
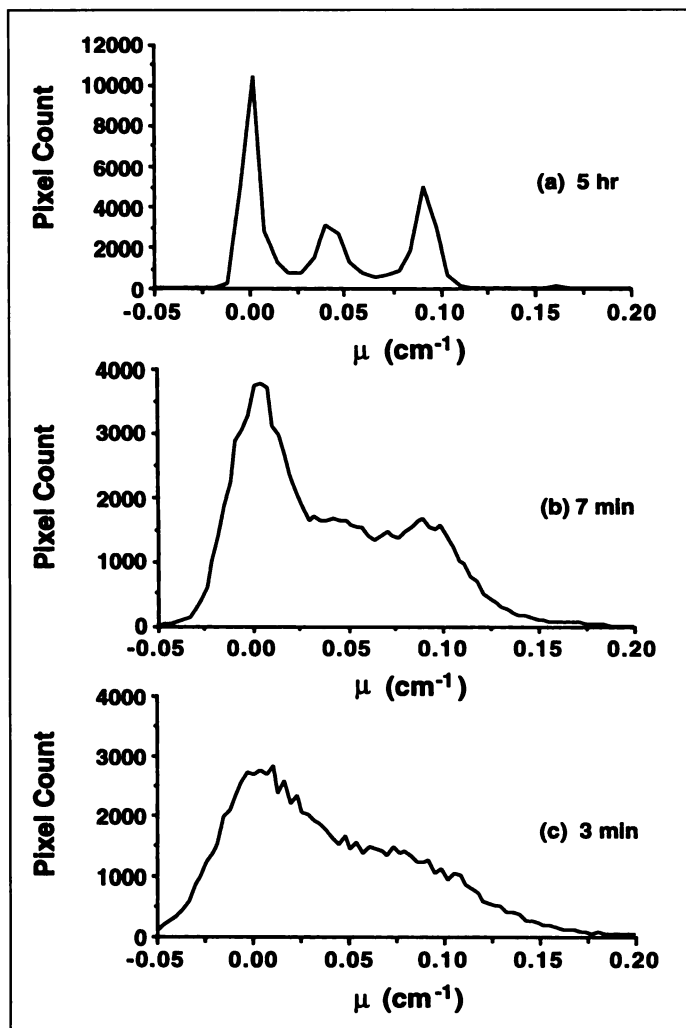

FIGURE 1. Measured attenuation histograms resulting from the phantom-based simulations corresponding to (A) 5-hr, (B) 7-min and (C) 3-min scan durations and 7-mm smoothing. The three distinct peaks in the 5-hr histogram are blurred due to noise in the 7-min and 3-min histograms (note the lower y-axis maximum values).

According to Eq. 6, $\hat{t}_j$ will be positive if its initial estimate is positive thereby guaranteeing no negative values for the estimated histogram $(8,9)$.

The histogram estimation used pixels inside a 118-pixel radius (including scanner table). Histogram parameters were varied to determine optimal values based on initial estimation trials. Bin numbers of 40 and 60 were investigated for n_t while varying n_m from 40 to 120 and algorithm iteration from 0.5K to 100K. The best tradeoff between algorithm convergence and computation time was obtained with $n_t = 40$, $n_m = 80$ and 50K iterations. The minimum and maximum μ values of all histograms were fixed to $-0.05\ \text{cm}^{-1}$ and $0.20\ \text{cm}^{-1}$, respectively. The measured and estimated bin widths were 0.003 cm^{-1} and 0.006 cm^{-1}, respectively.

Pixel Remapping. A diagram of the pixel remapping procedure is shown in Figure 2. The goal of this step is to produce an attenuation image with a histogram that matches the estimated histogram, $\hat{t}$. This was accomplished using the measured $(F_m(\mu))$ and estimated $(F_t(\mu))$ cumulative probability functions. A percentile value is determined for each measured pixel through interpolation of $F_m(\mu)$. Then, a new remapped pixel value (μ_r) is chosen which has the same percentile value in $F_t(\mu)$ as the original pixel, mathematically this is (Appendix A):

$$\mu_r = F_t^{-1}(F_m(\mu)). \qquad \text{Eq. 7}$$

In this manner, the rank order of the pixels in the attenuation image is maintained.

Reprojection. The complete array of ACFs was obtained by reprojection of the attenuation image. For each projection angle, the image was first rotated to match the projection angle, using bilinear interpolation. Pixel contributions to each projection ray were determined by column summation. The bin width in the projection array was the same as the pixel width in the attenuation image.

Reprojection can result in reduction of image resolution $(10,11)$ affecting the bias and noise in reconstructed data. Therefore, in
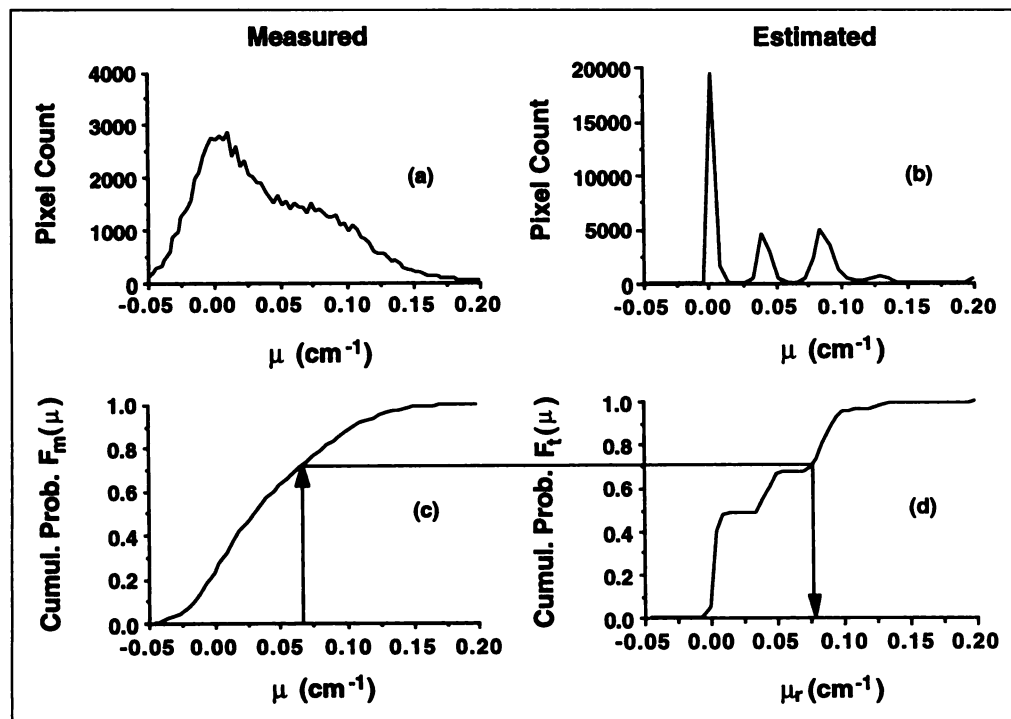
FIGURE 2. Prior to remapping, a maximum likelihood algorithm is applied to (A) the measured histogram to obtain (B) the estimated histogram. Pixel remapping is performed by: (1) computing (C) the measured and (D) the estimated cumulative probability functions $(F_m(\mu)$ and $F_t(\mu)$, respectively); (2) determining a percentile value for each measured pixel value (arrow in C); (3) mapping of the measured percentile to the estimated percentile curve (line between C and D); and (4) assigning a new μ value to that measured pixel (arrow in D). These histograms correspond to 3-min phantom data (7-mm FWHM smoothing, Case I).

order to distinguish between the effects of histogram sharpening with reprojection and reprojection alone, all emission images were also reconstructed with reprojected attenuation data (without histogram sharpening) for comparison to the histogram sharpening results. In the sections to follow, a "processed" attenuation image is one that has been histogram sharpened, remapped and reprojected. A "processed" emission image was reconstructed using processed attenuation data. An "unprocessed" emission image was reconstructed with attenuation data that has only been reprojected.

Data Analysis

Cardiac sector and ROI analyses were applied to the emission images. A user-defined myocardial ROI was divided into 12 sectors and the mean counts per sector (S) were used to assess bias.

Phantom Data: Sector Analysis. Mean sector count values from the high-count emission data that were reconstructed with the unprocessed high-count ACFs were taken as the reference (S^R) data for the bias calculations. Phantom percent differences (PPD_j) between the emission and reference data were calculated for each sector j across the 50 images:

$$PPD_j = \frac{\sum_{i=1}^{50} \left[\left(\frac{S_{i,j} - S_j^R}{S_j^R} \right) 100 \right]}{50}$$ Eq. 8

where $S_{i,j}$ is the sector value in realization i, sector j. Average bias ($\overline{PPD}$) was determined as the average value of the percent differences over all 12 sectors.

Absolute percent differences were computed using the average of the absolute sector values ($\bar{S}_P - \bar{S}_U$) with the unprocessed as reference. Relative sector values were then computed by normalizing the absolute counts for each sector to the average value for the 12 sectors (e.g. $S_i/\bar{S}$). A difference (P − U) was computed for each sector across the 50 realizations and means were determined for each sector.

Noise was assessed using the sector coefficient of variation (CV_j) which is the value of the standard deviation across the 50 replicate S_{ij} values divided by its reference, S_j^R. To obtain relative noise values, the average CV value over all 12 sectors ($\overline{CV}$) was normalized to the average value obtained from emission images reconstructed using unprocessed Case A data (lowest noise case).

Human Data: Sector Analysis. The 30-min emission data reconstructed with the unprocessed 15-min ACFs were used as reference data for the bias assessment. Differences were calculated between each emission S_j value and the reference value. Percent differences (HPD_j) were obtained for each sector j by dividing by the average reference S value:

$$HPD_j = \left(\frac{S_j - S_j^R}{\bar{S}^R} \right) 100$$ Eq. 9

and an average percent difference (n = 84, 7 slices, 12 sectors/slice) was calculated.

Absolute and relative differences between the processed and unprocessed human data were also examined. Absolute percent differences were computed using the average absolute sector values ($\bar{S}_P - \bar{S}_U$) with the unprocessed as reference. Relative differences were computed using the normalized sector data, as described for the phantom. A difference (P − U) was computed for each sector across the 7 slices and means were then determined for each sector.

Effective Time Gain. In contrast to the phantom, the evaluation of noise was not straightforward for the human data because noisy replicates were not available and emission image noise is primarily due to the emission data. A multi-step analysis that accounts for noise in the emission data was used to determine an effective time gain factor (α) that represents the increase in transmission scan duration that was effectively achieved by histogram sharpening.

In the first step, ROIs were used to estimate the emission image variance ($\sigma^2_{\Delta T}$) for each transmission scan duration (ΔT). Twenty-three ROIs were placed on the emission images in uniform regions of the phantom or human thorax. The pixel-to-pixel standard deviation determined for each region was normalized to the mean myocardial sector value for each image (SD_{bkg}/myo). None of the 23 ROIs was placed in the heart because the selective myocardial radioactivity uptake will cause the pixel-to-pixel standard deviations to reflect differences due to structure and partial volume effect as well as noise.

In the second step, the variance estimates were used to solve mathematically for α. As noted above, the emission image noise was fixed while the transmission image noise varied. For a given smooth level, the noise in the emission (σ_E) and transmission (σ_T) data add in quadrature (*3,12*) as follows:

$$\sigma^2_{\Delta T} = \sigma^2_E + \frac{\sigma^2_T}{\Delta T},$$ Eq. 10

where σ_T represents the noise from a 1-min transmission scan. For the unprocessed human transmission data, ΔT corresponds to a scan duration of 15 or 7 min and for the processed data, ΔT corresponds to the scan duration achieved by histogram sharpening (ΔT_{HS}). Therefore, variance values were determined for the 15-min (σ^2_{15}) and 7-min (σ^2_7) unprocessed and 7-min histogram-sharpened (σ^2_{HS}) emission images. Equation 10 was used to estimate σ^2_E and σ^2_T from the two emission image variances for the unprocessed data (σ^2_{15} and σ^2_7). These estimates and σ^2_{HS} were then used to estimate ΔT_{HS}. This analysis can be interpreted as using the three measurements of $\sigma^2_{\Delta T}$ to estimate three unknowns: σ^2_E, σ^2_T and ΔT_{HS}.

In the final step, the ΔT_{HS} parameter is normalized to the true transmission scan duration to provide the effective time gain, α:

$$\alpha = \frac{\Delta T_{HS}}{\Delta T}.$$ Eq. 11

The noise in the phantom data was also assessed using this type of ROI analysis. The average effective time-gain factor across the 50 replicates was determined for 3- and 7-min scans using the 15-min data as reference. In addition, the $\overline{CV}$ values determined for the 50 replicates were used as another measure of image noise to obtain effective time-gain factors.

RESULTS

Histogram Model

Figure 3 is a graph of the pixel standard deviation versus mean μ value for Case I (3 min/7 mm) phantom attenuation images with the line of best fit from the linear regression of these data (r = 0.73) that provides σ_s and σ_0 in Equation 3. The linear correlation coefficients were uniform (r = 0.73 ± 0.01, n = 9) across the scan durations and smooth levels for the phantom. The data for Figure 3 correspond to 100 pixels that were subsampled from the mean and standard deviation images.

A linear model was also used for the human transmission data, although the mean correlation coefficient was lower (r = 0.51 ± 0.21, n = 9). However, the mean σ_s and σ_0 values were similar for the phantom (n = 50) and human (n = 3) data. Case B and Case H values for the phantom were σ_s = 0.0318, σ_0 = 0.0007 and σ_s = 0.0613, σ_0 = 0.0013 with corresponding human values of σ_s = 0.0312, σ_0 = 0.0007 and σ_s = 0.0579, σ_0 = 0.0014. As expected, σ_0 and σ_s were found to be inversely proportional to the square root of the scan time.
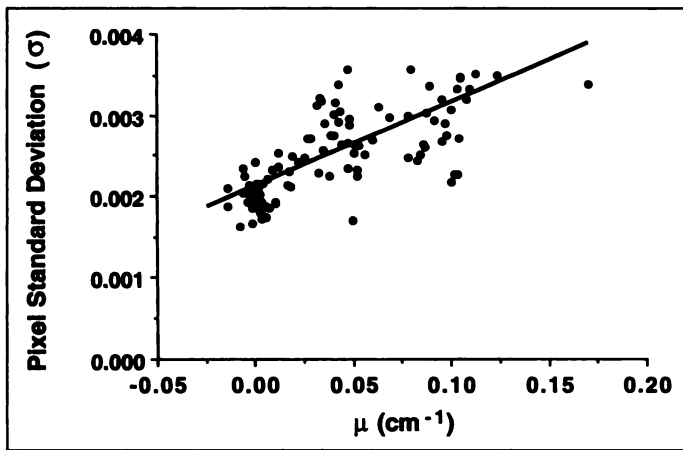
FIGURE 3. Pixel standard deviation (σ) versus the mean pixel value (μ) from mean and standard deviation (n = 50) phantom attenuation images (Case I). A linear regression of these data (r = 0.73) provides the slope (σ_s = 0.103) and y-intercept (σ_0 = 0.002) for the noise function described in Equation 3. These data were subsampled from the mean and standard deviation images (to 100 pixels).

Histogram Estimation (Histogram Sharpening)

Phantom Data. Figure 4 shows typical phantom results for the measured (dashed line) and estimated (solid line) attenuation histograms obtained after processing of a Case I attenuation image. The histogram sharpening method extracted three distinct peaks that correspond to air, lung and soft tissue. Two lesser peaks (about 2% of total pixels) are also seen with an average bin value of 0.165 cm^{-1} that agrees with the mean ROI value of 0.164 cm^{-1} for the simulated spine in the reference attenuation image. The means of the estimated histograms (n = 50) generally display three distinct peaks that correspond to bin values of 0.002 cm^{-1}, 0.040 cm^{-1} and 0.090 cm^{-1}. However, individual histograms sometimes represented the lung and, occasionally, the soft tissue by multiple peaks (see Discussion).

Figure 5 shows typical phantom attenuation images corresponding to unprocessed (top row) and processed (bottom row) data. In contrast to the unprocessed images, the histogram-sharpened images display more uniform gray levels, as expected from the estimated histograms (Fig. 4). Accordingly, the processed emission images shown in Figure 6 display some noise reduction in the myocardium (first and fourth rows) and
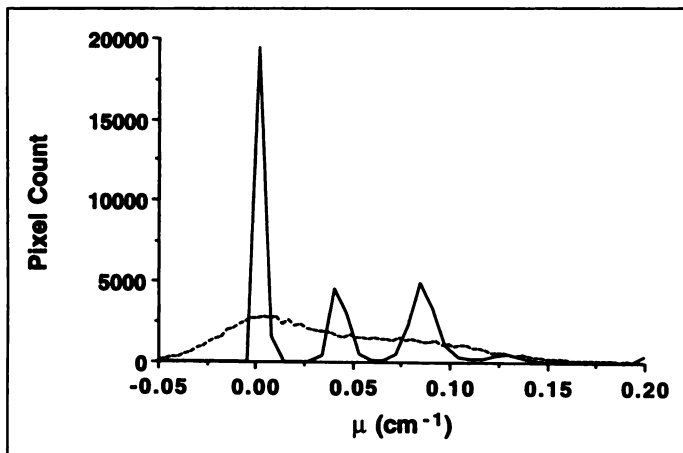

FIGURE 4. Measured (dashed line) and estimated (solid line) phantom histograms obtained after histogram sharpening of an attenuation image (Case I). The method was able to extract three distinct peaks that correspond to air, lung and soft tissue with no a priori assumptions of the underlying μ values. Two lesser peaks that may correspond to the simulated spine are also seen. The number of bins in the measured and estimated histograms were 80 and 40, respectively.
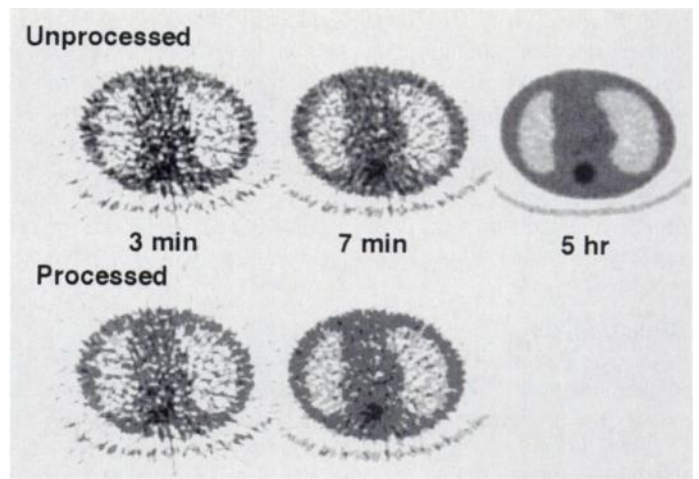

FIGURE 5. Unprocessed (top row) and processed (bottom row) phantom attenuation images corresponding to 3-min (Case I), 7-min (Case H) and 5-hr (reference) transmission data. Processing results in a more uniform gray level as expected from the estimated histograms (Fig. 4). The images are displayed on a common scale using the maximum value of the 3-min processed image.

surrounding tissue (second and third rows) with no visually apparent artifacts. The transmission data is the primary source of noise in the phantom emission images, as can be seen for the data corrected with the 5-hr transmission scan.
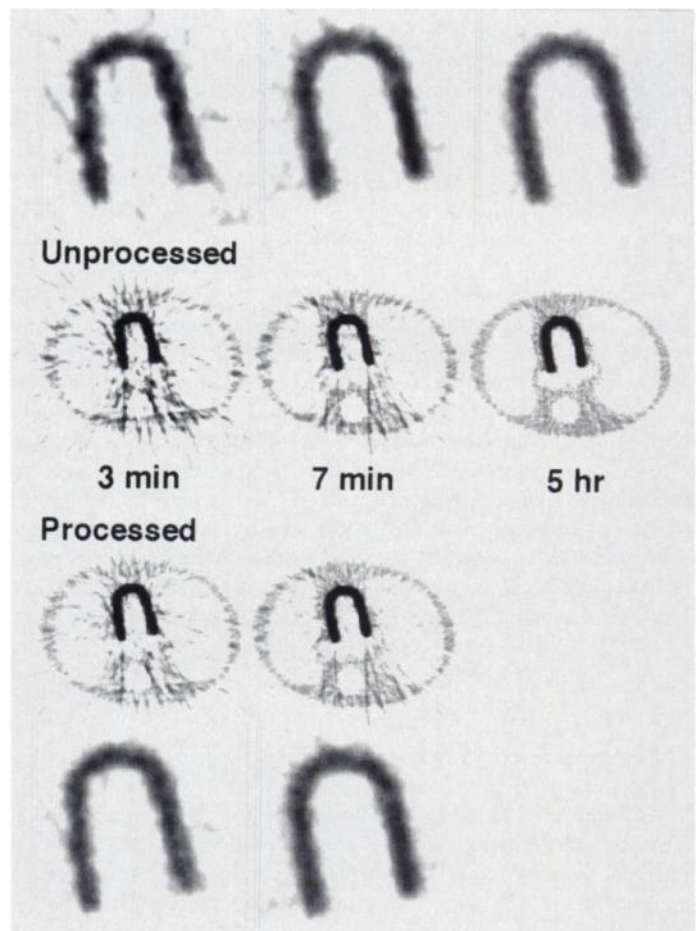

FIGURE 6. The phantom emission images that were reconstructed with the attenuation data of Figure 5, with zoomed images of the simulated myocardium (first and fourth rows). Qualitatively, the processed images appear less noisy both in the surrounding tissue (third row) and myocardium (fourth row) with no apparent artifacts. The zoomed images are displayed with respect to the 3-min unprocessed maximum and the original images are displayed on a scale well below all image maximas to accentuate the background.
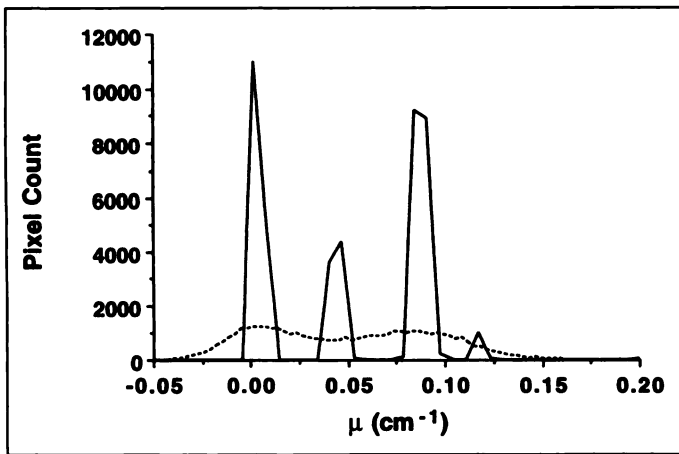
FIGURE 7. Measured (dashed line) and estimated (solid line) histograms for the central slice of a Case H (7-min/7-mm) attenuation image for one of the human subjects (Subject 1). The three distinct peaks that correspond to air, lung and soft tissue are distinguishable with a lesser peak that may correspond to bone.

Human Data. The measured and estimated attenuation histograms are shown for one of the human subjects (Subject 1) in Figure 7. These data correspond to the central slice of a Case H attenuation image. As observed for the phantom, histogram sharpening produced air, lung and soft tissue peaks with a lesser peak that may correspond to bone (0.12 cm^{-1}). Variability in the estimated histograms as demonstrated by multiple lung and soft tissue peaks, was also seen with the human data. The estimated histograms across subjects and smooth levels, display lung and soft tissue peaks that range in μ value from 0.021 cm^{-1} to 0.053 cm^{-1} and from 0.072 cm^{-1} to 0.090 cm^{-1}, respectively, with a well-determined air peak at 0.002 cm^{-1}.

Figure 8 shows the unprocessed and processed attenuation (first column) and emission (second column) images for this subject's central slice (Case H) along with the reference images (third column). Similar to the phantom, the processed attenuation image appears more uniformly gray and the corresponding emission image appears to be less noisy with no apparent artifacts. Noise reduction in the final human emission images is less visible than that for the phantom study since the emission data is the primary source of image noise in these studies.
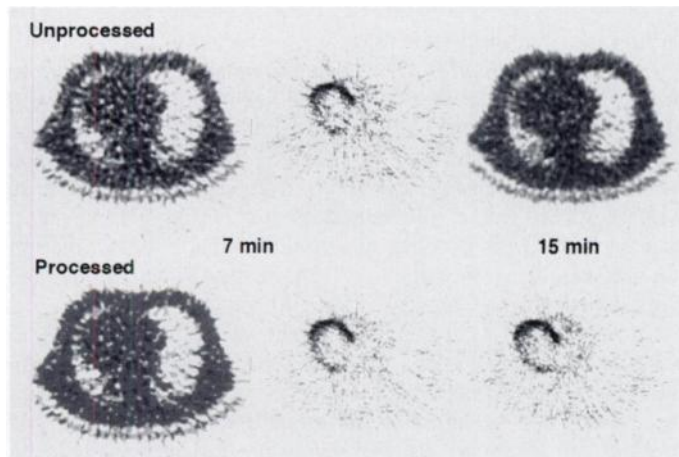

FIGURE 8. Attenuation images (first column) with corresponding emission (second column) and 15-min reference images (third column) for one human subject (Subject 1: Case H). The processed attenuation image is more homogeneous and some noise reduction is visible in the processed emission image with no apparent artifacts. The attenuation and emission images are displayed on different common scales, with respect to the 7-min processed image maximum.
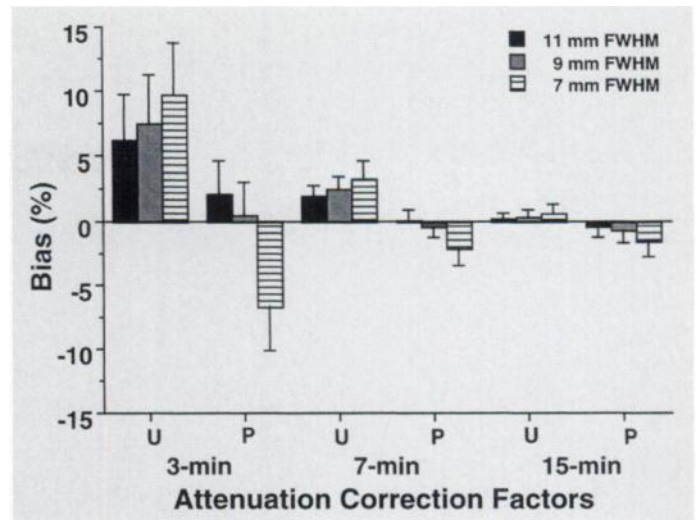

FIGURE 9. The phantom emission bias (across 12 sectors) from images corresponding to 3-, 7- and 15-min unprocessed (U) transmission data at three levels of smoothing. The unprocessed images were positively biased (maximum: 10%, Case I). Processing (P) reduces the positive bias with increasingly negative biases with decreasing FWHM (maximum: 7%, Case I).

Data Analysis

Phantom Data: Sector Analysis. The phantom sector results are presented in Figure 9 and Table 2. The bias ($\overline{PPD}$) and its standard deviation across the 12 sectors for emission data reconstructed with the 3-, 7- and 15-min unprocessed (U) data is shown in Figure 9. The unprocessed images are positively biased (Case A, 15 min/11 mm: 0.3 $\pm$ 0.5%; Case I, 3 min/7 mm: 9.8 $\pm$ 4.0%). Processing (P) reduced the positive bias and introduced a negative bias (Case A: -0.5 ± 0.8%; Case I: -6.6 ± 3.4%) that is larger for the noisier cases. The change in bias (P $-$ U) for cases of intermediate noise level (C, E and G) was about 3–4% while that for Case I (the noisiest case) was about 16%. The positive bias in the unprocessed images is attributed to noise in the transmission data and its reduction after processing is attributed to noise reduction and to inherent properties of the sharpening method (see Discussion).

Normalized sector differences averaged across the 50 realizations revealed sinusoidal difference curves with maxima and minima that were very close in magnitude. The largest difference was observed for sectors corresponding to the base and apex of the cardiac phantom. The greatest value (-6 ± 3%) corresponded to the shortest scan duration and lowest smooth level, as is consistent with the bias results in Figure 9. Except for the highest noise cases, the histogram sharpening method introduces a small bias in relative sector differences of <3%.

Relative emission noise values ($\overline{CV}$) are shown in Table 2.

TABLE 2
Phantom Relative Emission Noise[*][†]

FWHM		Transmission scan duration		
		15 min	7 min	3 min
11 mm	Unprocessed	100	155	249
	Processed	72	107	185
9 mm	Unprocessed	112	175	286
	Processed	76	118	202
7 mm	Unprocessed	125	199	334
	Processed	85	137	209

[*]Noise values: $\overline{CV}$ for myocardial sectors across 50 replicates.
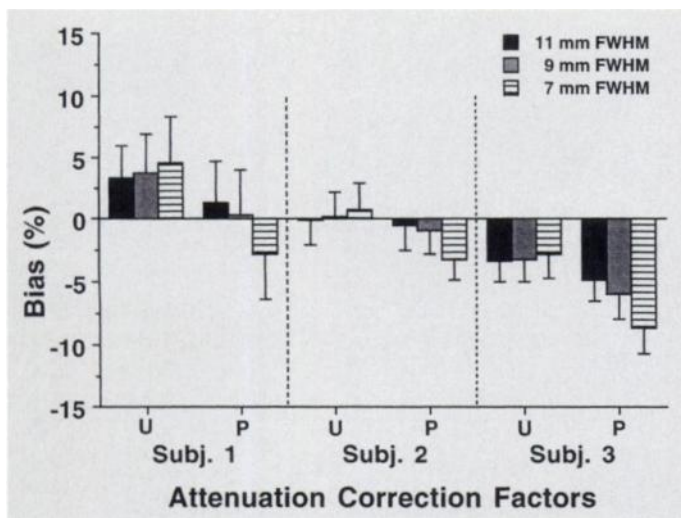[†]Noise values were normalized to 15 min-11 mm (Case A) value.

FIGURE 10. The human emission bias (across 7 slices and 12 sectors) corresponding to unprocessed (U) and processed (P) 7-min transmission data at three levels of smoothing. Generally, biases were positive for Subjects 1 and 2 (maximum: 4.5%) before processing and negative after processing (maximum: -3.1%). For Subject 3, negative biases were observed before (maximum of -3.4%) and after (maximum of -8.7%) processing.

Histogram sharpening resulted in a consistent reduction (31 ± 3%) of relative noise across the scan durations. The noise in the emission images is primarily transmission noise due to the high-count phantom emission data. Therefore, Table 2 also shows that the relative noise value obtained for a processed emission image is comparable to that for an unprocessed image for which the transmission scan duration is about 100% greater; in other words, the relative noise value for a 7-min processed case is close to that for a 15-min unprocessed case. Alternatively, this means that less smoothing could be performed, i.e., the relative noise value for a 7-mm processed case is less than that for an 11-mm unprocessed case.

Human Data: Sector Analysis. The bias determined across the 7 central images for each human subject is shown in Figure 10. Biases of the unprocessed 7-min data with respect to the 15-min reference values were variable. One might expect this from noise and possible motion between transmission scans. Processing produced more negative biases, particularly for the 7-mm case. The human bias patterns are similar to those obtained for the 7-min phantom data (Fig. 9) as is especially evident for Subject 1.

The human absolute sector differences agree with the phantom results. A maximum difference was observed at 7-mm smoothing (Subject 1: -7.2%) with middle range (Case E) differences of -3.4, -1.1 and -2.9% for Subjects 1–3, respectively. The normalized sector differences for Case E were -6.0 ± 5.0, -4.2 ± 2.5% and -2.6 ± 5.0 for Subjects 1–3, respectively (across 7 slices).

Effective Time Gain (α). Mean values of α were calculated using data pooled across scan duration and smooth level. The values were similar for the phantom ROI (1.55 ± 0.22, n = 6) and human ROI (1.50 ± 0.35, n = 9) data. The ROI α values show that the noise of a processed emission image is comparable to that for an unprocessed image for which the transmission scan duration is about 50% greater. However, α values determined from the phantom $\overline{CV}$ value (50 realizations) were greater (1.96 ± 0.19, n = 6), i.e., a 100% gain in scan duration may be achievable. There is a difference between the magnitude of the effective time gain assessed by ROI interpixel variance and by sector variances determined across replicates (see Discussion).

DISCUSSION

The goal of this study was to improve PET chest attenuation correction through the histogram sharpening of attenuation images. The results show that histogram sharpening achieves a 50–100% increase in the effective transmission scan duration. Alternatively, it allows less smoothing of the transmission data (e.g., 7 mm rather than 11 mm) without an increase in noise.

Model Assumptions

Distribution of μ Values. In this work, no underlying distribution of μ values was assumed. This is an advantage of the method due to the finite spatial resolution of the attenuation image. This is important at regional borders where pixels have mixed attenuation and when respiratory motion during the scan can cause pixels to have an effective μ value that is actually a combination of that for lung and soft tissue. Therefore, not all pixels should be assigned to the ideal μ values of air, lung and soft tissue.

Noise Function. Initially, a uniform standard deviation was assigned to all pixels based on an average pixel-to-pixel standard deviation determined from ROI sampling of the attenuation image. In this case, the mean estimated histogram for Case I displayed peaks that were incorrectly shifted toward higher bin values, especially for lung. A linear noise model was then investigated and the histograms estimated from noisy data were greatly improved. The slope and y-intercept values determined for the noise model were similar for the phantom and human data, although the correlation coefficient was lower for the human data. This may be due to increased noise in the standard deviation values obtained from the interpixel variance (rather than across 50 phantom replicates) or by the more complex attenuating media in the patients.

The estimated histograms occasionally displayed multiple peaks for the lung, soft tissue and bone. This occurred less often for the noisier cases. This may be due to oversimplifications in the noise model, i.e., not accounting for spatial variation in the transmission image noise, and may contribute to the negative bias introduced by histogram sharpening in some cases. This algorithm could be improved if an analytic formula for attenuation image noise could be derived, as has been done for emission images (*12,13*). In this case, each individual pixel's μ_i and σ_i values could be used to explicitly account for the noise characteristics of the image. Use of this data would require modification of the algorithm to directly use individual μ values instead of a measured image histogram.

Attenuation Image Processing

Histogram Estimation (Histogram Sharpening). The estimation of the true histogram could have been accomplished using other algorithms such as deconvolution, Newton-Raphson method or Fisher Scoring (*14*). An EM algorithm was chosen for this work because of the positivity guarantee and the ease with which it was implemented in our setting. However, a drawback of EM is its slow convergence (histogram estimation required about 5 min per slice (VAXstation, 3100 Model 76, Digital Equipment Corp. Marlboro, MA).

Currently this algorithm requires the definition of ROIs to estimate attenuation image noise. If the attenuation pixel noise function is determined to be similar for all human studies (accounting for transmission source activity) or if an analytic formula can be included, then the image processing could be completely automated.

Pixel Remapping. The remapping algorithm creates a new attenuation image based on the rank order of pixels in the measured attenuation image. Therefore, the processed and unprocessed images have similar noise patterns (see Fig. 5). Some pixel misplacement is inherent in the remapping algo-

rithm, i.e., a pixel in the lung may have a higher μ value than a tissue pixel due to noise. In that case, the lung pixel may be assigned a μ value close to tissue and the tissue pixel would be assigned a μ value close to lung. This aspect of the remapping step is seen in Figure 5 as patches of wrong values in the lungs of the 3-min image. These effects are also present in other attenuation correction methods which use histograms (5,6).

Reprojection. Reprojection alone affects sector values. Therefore, the phantom sector biases were computed using reprojected unprocessed data. However, only small changes were observed in the $\overline{CV}$ values of the original and reprojected reference phantom data (data not shown). These findings agree with those of Ollinger et al. (*10*) who reported that the transmission sinogram variance reduction that results from reprojection does not produce a corresponding reduction in emission image noise.

It is possible that inconsistencies in the projection data could arise with inaccuracies in the interpolation step. However, inconsistencies also arise from statistical noise in the projection data and it is likely that such effects are more significant than the inconsistency introduced by reprojection sampling errors.

Data Analysis

The bias assessment demonstrated positive biases for the unprocessed emission images relative to the reference data and this is attributed to transmission data noise. A complete description of this positive bias is provided by Freedman et al. (*15*). Briefly, the value of a given ACF is equal to B/T. If the blank scan is of long scan duration (noise-free) then the noise in the ACF is due to variance in T. The transmission sinogram pixel value (T) will be Poisson-distributed, $T \sim$ Poisson (μ_T). Taylor series expansion of B/T about the mean of T gives:

$$B/\mu_T - (T - \mu_T)B/(\mu_T)^2 + (T - \mu_T)^2 B/(\mu_T)^3$$

$$+ \text{ higher order terms.}$$

The expected value of B/T is then:

$$B/\mu_T[1 + \sigma^2(T)/(\mu_T)^2].$$

Therefore, the expected value of the ACF will always be greater than the mean value by an additive term that is proportional to the coefficient of variation of the transmission counts. Noisy transmission data will cause the emission data to be multiplied by ACFs that are too large, thus causing the positive biases in the unprocessed data. Histogram sharpening reduced the positive bias compared to the unprocessed data, consistent with a lower noise level in the processed data. However, histogram sharpening also introduced negative biases, particularly in the noisiest cases. This may be due to pixel misplacement by the remapping step.

General Points. Overall the histogram sharpening method performed well across the phantom and human data demonstrating noise reduction across all smooth levels. The phantom and human ROI α values are 1.5 and the phantom relative noise α value is 2. It is possible that this difference is due to spatial variations in the image noise since the background ROI data were derived throughout the image while the $\overline{CV}$ values are based solely on data from the myocardium.

The absolute and normalized sector differences were <4% for all but the noisiest cases. The human results are more variable but consistent with the phantom results. A larger cohort of patients is needed to assess this bias more accurately. It is also difficult to assess from three human studies, when a decrease in noise at a fixed resolution is more appropriate than improved resolution at a fixed noise; this also requires other

types of patient studies (e.g., blood flow) and physician assessment. It is not clear how histogram sharpening will perform for slices of the human studies where the attenuation histograms differ greatly from those studied here. Other questions to address include: (a) would histogram sharpening method be effective for brain transmission scans? (b) is the method applicable to SPECT images for which the attenuation peaks are better separated at lower energies?

CONCLUSION

The histogram sharpening method of attenuation correction can reduce the noise that is propagated from the transmission data to the emission image with small biases (<4%). The noise in a processed emission image is comparable to that for an unprocessed image for which the transmission scan duration is 50–100% longer. Alternatively, histogram sharpening permits less transmission data smoothing without increased noise.

APPENDIX

The new attenuation image is created via pixel remapping. Let ϕ be the mapping function that is applied to the measured pixel values (μ_m) to obtain the remapped pixel values (μ_r):

$$\mu_r = \phi(\mu_m). \qquad \text{Eq. A1}$$

The function $\phi(\mu)$ is determined through the use of the cumulative probability distribution functions of the measured:

$$F_m(\mu) = P(\mu_m \leq \mu) = \int_{-\infty}^{\mu} m(s)\, ds \qquad \text{Eq. A2}$$

and estimated:

$$F_t(\mu) = P(\mu_t \leq \mu) = \int_{-\infty}^{\mu} \hat{t}(s)\, ds \qquad \text{Eq. A3}$$

histograms. If ϕ^{-1} is the inverse mapping function ($\phi^{-1}(\mu_r) = \mu_m$) then

$$F_m(\mu) = P(\mu_m \leq \mu) \qquad \text{Eq. A4}$$

$$= P(\phi^{-1}(\mu_r) \leq \mu) \qquad \text{Eq. A5}$$

$$= P(\mu_r \leq \phi(\mu)) \equiv F_r(\phi(\mu)) \qquad \text{Eq. A6}$$

since ϕ is monotonic. Next, we require that the μ values of the remapped and estimated cumulative probability distribution functions are equal, such that:

$$F_r = F_t \qquad \text{Eq. A7}$$

so

$$F_t(\phi(\mu)) = F_m(\mu) \qquad \text{Eq. A8}$$

and therefore,

$$\phi(\mu) = F_t^{-1}(F_m(\mu)). \qquad \text{Eq. A9}$$

REFERENCES

1. Huang S-C, Hoffman EJ, Phelps ME, Kuhl DE. Quantitation in positron emission tomography: 2. effects of inaccurate attenuation correction. *J Comput Assist Tomog* 1979;3:804–814.

2. Palmer MR, Bergstrom M, Pate BD, Beddoes MP. Noise distribution due to emission and transmission statistics in positron emission tomography. *IEEE Trans Nucl Sci* 1986;33:439–442.
3. Dahlbom M, Hoffman EJ. Problems in signal-to-noise ratio for attenuation correction in high resolution PET. *IEEE Trans Nucl Sci* 1987;34:288–293.
4. Huang SC, Carson RE, Phelps ME, Hoffman EJ, Schelbert HR, Kuhl DE. A boundary method for attenuation correction in positron computed tomography. *J Nucl Med* 1981;22:627–637.
5. Xu EZ, Mullani NA, Gould KL, Anderson WL. A segmented attenuation correction for PET. *J Nucl Med* 1991;32:161–165.
6. Meikle SR, Dahlbom M, Cherry SR. Attenuation correction using count-limited transmission data in positron emission tomography. *J Nucl Med* 1993;34:143–150.
7. Abramowitz M, Stegun IA. *Handbook of mathematical functions.* New York: Dover Publications; 1968.
8. Shepp LA, Vardi Y. Maximum likelihood reconstruction for emission tomography. *IEEE Trans Med Imag* 1982;1:113–122.
9. Lange K, Carson R. EM reconstruction algorithms for emission and transmission tomography. *J Comput Assist Tomog* 1984;8:306–316.
10. Ollinger JM. Reconstruction-reprojection processing of transmission scans and the variance of PET images. *IEEE Trans Med Imag* 1992;39:1122–1125.
11. Yu D-C, Huang S-C. Study of reprojection methods in terms of their resolution loss and sampling errors. *IEEE Trans Nucl Sci* 1993;40:1174–1177.
12. Alpert NM, Chesler DA, Correia JA, et al. Estimation of the local statistical noise in emission computed tomography. *IEEE Trans Med Imag* 1982;1:142–146.
13. Huesman RH. A new fast algorithm for the evaluation of regions of interest and statistical uncertainty in computed tomography. *Phys Med Biol* 1984;29:543–552.
14. Kendall Sir M, Stuart A. *The advanced theory of statistics.* New York: Macmillan; 1979:52–53.
15. Freedman NMT, Bacharach SL, Carson RE, Price JC, and Dilsizian V. Effect of smoothing during transmission processing on quantitative cardiac PET. *J Nucl Med* 1996: in press.

NUCLEAR CARDIOLOGY: CURRENT PERSPECTIVE

Myocardial Viability: Unresolved Issues

Abdulmassih S. Iskandrian

The Philadelphia Heart Institute, Presbyterian Medical Center, Philadelphia, Pennsylvania

The determination or assessment of myocardial viability has, over the past decade, captured the imagination and interest of many investigators in basic and clinical research using state-of-the-art technologies such as PET, SPECT, MRI and two-dimensional echocardiography (2-DE) (*1–12*). The emphasis in these studies has been to determine the absolute and comparative accuracy of these techniques (*1–3*). There are recent studies addressing the evaluation of the effect of viability assessment on patient outcome (*13–17*). The use of biochemical agents and other imaging methods in viability assessment is complex with many unresolved issues (Table 1) to be considered in the design and implementation of clinical protocols and in routine patient care.

DEFINITION

The issue of myocardial viability is most important in the presence of left ventricular (LV) dysfunction. Viable myocardium may be normal, hibernating or stunned while nonviable myocardium represents scar (*1–3*). Thus, hibernating myocardium is viable but viable myocardium is not necessarily hibernating. Hibernation refers to systolic LV dysfunction in the presence of hypoperfusion that recovers after coronary revascularization (*1,2,18*). It may represent a downregulation of contractile function in response to reduced resting myocardial blood flow. Stunned myocardium refers to systolic LV dysfunction that persists after an ischemic episode despite restoration of flow (*19*). The distinction between viability and hibernation is important to the understanding of differences between various diagnostic methods that use different markers such as flow, metabolism or function. The flow-metabolism mismatch pattern determined by PET (which reflects reduced resting flow but preserved, albeit altered, metabolism) represents the mainstream description of the pathophysiological changes in hiber-

nation (*6,20*). A recent study (*21*), however, raised doubt about the reliability of determining absolute rates of myocardial glucose uptake using the glucose tracer analog ^{18}F-deoxyfluoroglucose (*21*). The presence of redistribution (reversible defect) on rest-redistribution thallium imaging is also consistent with hypoperfusion and reduced resting flow (*5,16,17*) in viable myocardium. The recovery of regional dysfunction in such segments after coronary revascularization is also consistent with hibernation. On the other hand, the presence of redistribution on stress images or the presence of mild fixed thallium defects, mild fixed sestamibi defects or improvement in wall motion during inotropic stimulation (such as dobutamine) do not fulfill the same criteria for hibernating myocardium because it may be that mild fixed perfusion defects represent viable myocardium but are not markers of hibernating myocardium (*8,9,17*). A good example is subendocardial infarction with admixture of scar and normal myocardium in the infarct zone. The subepicardial myocardium is viable but does not have to be hibernating and this zone may very well respond to inotropic stimulation. If LV dysfunction is due to hibernation, it potentially may recover after coronary revascularization while such recovery may not be expected if the dysfunction is due to subendocardial scarring. This may explain the reason why improvement in wall motion on echocardiography with dobutamine has not been a specific marker of recovery of LV function after revascularization (*22*).

A similar issue may be raised with perfusion imaging. For example, Figure 1 depicts the resting myocardial perfusion on a radionuclide tomogram; area 1 is a region with normal tracer uptake; area 2 is a region with mild fixed defect; area 3 is a region with severe fixed defect and area 4 is a region with

TABLE 1
List of Unresolved Issues in Myocardial Viability

1. Definition of viable myocardium
2. Quantification of viable myocardium
3. Correlation between perfusion and function
4. Patient selection
5. Time of follow-up assessment
6. Completeness of revascularization
7. Perioperative myocardial infarction
8. Endpoints